Reprinted from Journal of the Optical Society of America B, Vol. 4, page 635, May 1987

Time-resolved spectra in the 80–340-Å wavelength region from Princeton Large Torus tokamak plasmas

J. H. Davé

Applied Research Corporation, 8201 Corporate Drive, Landover, Maryland 20785

U. Feldman and J. F. Seely

E. O. Hulburt Center for Space Research, Naval Research Laboratory, Washington, D.C. 20375-5000

A. Wouters, S. Suckewer, E. Hinnov, and J. L. Schwob*

Princeton Plasma Physics Laboratory, Princeton University, Princeton, New Jersey 08544

Received September 2, 1986; accepted January 5, 1987

High-resolution spectra from the Princeton Large Torus plasma have been recorded by a 2-m Schwob–Fraenkel soft-x-ray multichannel spectrometer. Spectra covering a wavelength range of approximately 50 Å were recorded every 50 msec, and the spectra were normalized and added together to produce composite spectra covering the region 80–340 Å. Several well-known reference lines were used to establish an absolute wavelength scale, and transition wavelengths were measured to an accuracy of approximately 0.02 Å. By subtracting spectra recorded at various times throughout the discharge, transitions from ions formed in the cooler and hotter plasmas were easily distinguished, and blends between hot and cold transitions were resolved. Wavelengths of transitions in C, O, Ti, Cr, Mn, Fe, and Ni have been measured.

INTRODUCTION

The study of the soft-x-ray spectroscopy of tokamak plasmas is important for the understanding of impurity concentrations, particle transport, and radiation losses (for a review, see Ref. 1). The H-, He-, and Li-like resonance transitions of the light impurities C and O and the $\Delta n = 0$ ground-state transitions of the highly ionized metallic impurities such as Ti, Cr, Fe, and Ni appear in the XUV spectral region. The spectra of elements that do not occur naturally in tokamak plasmas can be studied by injecting the elements using the laser blow-off technique.

The unambiguous identification of the transitions, particularly the transitions in the heavy ions, requires the observation of a number of lines from each ionization stage. The time dependence of the radiation is useful in distinguishing transitions in ions that occur over a range of electron temperature, and high spectral resolution is necessary to resolve blends of closely spaced lines.

Suckewer and Hinnov[2] measured the intensities of a number of allowed transitions in the wavelength range 90–300 Å from Fe XVIII, Fe XX, and Fe XXII. Stratton *et al.*[3] observed $\Delta n = 0$ transitions below 200 Å from Ti, Cr, Ni, and Ge with a spectral resolution of 0.7 Å.

In this paper, we present time-resolved spectra that were recorded by the 2-m Schwob–Fraenkel soft-x-ray multichannel spectrometer at the Princeton Large Torus (PLT) tokamak.[4–8] These spectra represent significant improvements in spectral resolution and wavelength coverage. An accurate wavelength scale was established using well-known reference lines and the geometry of the instrument. This accurate wavelength scale was essential for the identification of many of the transitions and also permitted the precise comparison of spectra recorded at various times during the same discharge and from different discharges. The signal-to-noise ratio was improved by adding a number of spectra, and many blends between transitions in ions that occur during the cooler and hotter periods of the discharge were resolved by subtracting spectra recorded during these periods.

We discuss in detail the establishment of the absolute wavelength scale over the wavelength region 80–340 Å. This includes the corrections for the distortions introduced by the flat multichannel plate detector, the nonlinearities in the optical-fiber transmission lines, and the electronic noise. We present the spectra of the intrinsic elements C, O, Ti, Cr, Fe, and Ni. The spectra of the elements injected by the laser blow-off technique will be presented in a separate paper.

EXPERIMENTAL DETAILS

The PLT tokamak produces plasma with central electron densities up to 1×10^{14} cm^{-3} and central electron temperatures up to 2.5 keV in ohmically heated discharges. The plasmas typically have durations of somewhat less than 1 sec.

The plasma was viewed radially by a 2-m grazing-incidence spectrometer.[4] The spectrometer was fitted with a 600-line/mm grating, and the wavelength coverage was 5–340 Å for a grating blazed at 1°31′ or 20–340 Å for a grating blazed at 3°39′. The spectra were recorded by either one or two flat MgF_2-coated microchannel plates (MCP's) that were interferometrically adjusted to be tangent to the Row-

0740-3224/87/050635-09$02.00

land circle. Each MCP was fitted with a phosphor-screen image intensifier and coupled by a flexible fiber-optic conduit to a 1024-element photodiode array. The photodiode array was controlled and read out by an optical multichannel analyzer. Each MCP was capable of covering a wavelength range of 20 Å at short wavelengths or up to 70 Å at the long-wavelength limit. High spectral resolution and relatively low background were achieved over the entire wavelength range. The widths of isolated spectral lines were typically 0.2 Å at 20 Å and 0.3 Å at 300 Å.

Spectral scans were recorded at intervals of 50 msec throughout the PLT discharge. Typically 10 usable scans with strong spectral lines were obtained on each discharge. Spectral lines from ions that are formed at low electron temperatures appear intense in the first few scans of a discharge. These cold lines diminish as the ohmic heating proceeds. During the subsequent plateau regime, when the electron temperature and density are approximately constant, the hot lines are much more intense than the cold lines.

DATA REDUCTION

A typical example of the data recorded during the plateau regime is shown as trace (a) in Fig. 1. The MCP detector was positioned to record data between 210 and 222 Å, and trace (a) shows the counts recorded by pixels number 500 through 700 of the detector array. Superimposed upon the spectral data is a periodic noise pattern that originates in the electronic components of the photodiode-array detector. The period of the noise pattern for the wavelength region of Fig. 1 is four pixels, and this corresponds to a wavelength range of 0.1–0.3 Å, depending on the wavelength region. Since the period of the noise pattern is comparable with the width of the spectral lines, it is not possible to smooth out the noise pattern without spoiling the spectral resolution. The data recorded after the end of the discharge are pure noise, and the noise pattern recorded on adjacent scans

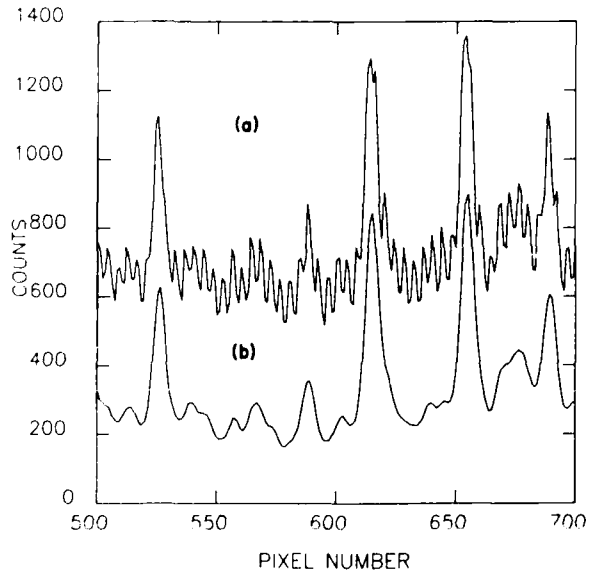

Fig. 1. The spectral data as a function of pixel position covering the wavelength region 210–222 Å. The unprocessed data are shown in (a), and the electronic background noise has been removed in (b).

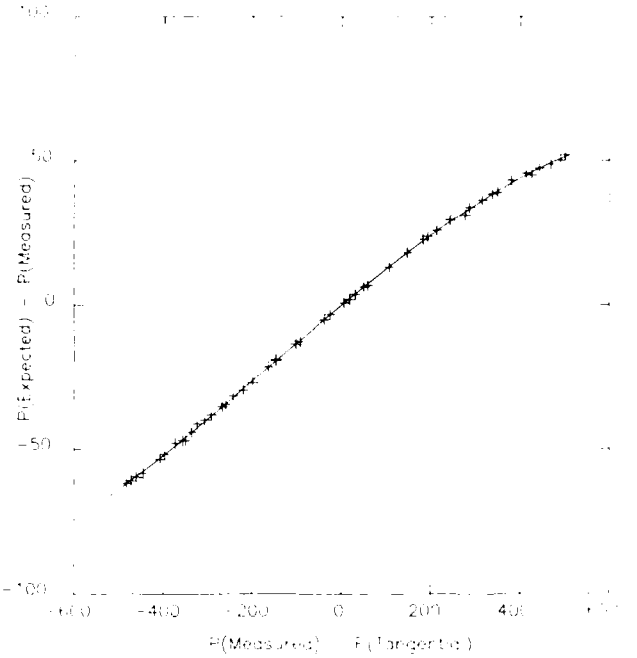

Fig. 2. The calibration curve for the MCP. The ordinate is the difference between the expected and the measured pixel positions of the reference spectral lines, and the abscissa is the difference between the measured and the tangential pixel positions.

during this time does not change in pixel position. Shown in trace (b) of Fig. 1 is the spectrum that remained after the noise pattern was subtracted from the data of trace (a). The differences between traces (a) and (b) are significant, and the subtraction of the noise pattern is essential for the establishment of an accurate wavelength scale.

The wavelength scale can be determined from the well-known relation

$$\lambda = d(\cos\alpha - \cos\beta), \tag{1}$$

where λ is the wavelength, d^{-1} is the number of lines per unit length of grating, α is the angle of incidence, β is the angle of diffraction, and β_0 is the angular position of the MCP pixel that is tangent to the Rowland circle. A detailed description of the experimental geometry is given in Appendix A (see Fig. 12 below).

The wavelengths for the well-known standard lines that were obtained from the above equation were initially found to be slightly different from the accepted values. Two different factors contributed to the sizable errors in the measured wavelengths. The fiber-optic taper between the MCP and the detector introduced a nonlinear dispersion in pixel position that increases as a function of distance from the tangential pixel. Second, the measured values of the angular position β_0 of the tangential pixel were not so accurate.

To correct for these discrepancies, a calibration curve for pixel position was obtained in the following manner. For each experimental run, the pixel positions of the standard lines were measured by fitting Gaussian profiles. The expected pixel positions of the lines were calculated from the known wavelengths (see Appendix A), and the differences between the measured and expected pixel positions were graphed as a function of pixel position as shown in Fig. 2. Such a calibration curve was generated for each MCP posi-

tion. The angular positions β_0 were adjusted slightly from the experimentally measured values so that the calibration curves for each MCP position had the same shape. A final calibration curve was obtained by fitting a least-squares polynomial, and this calibration curve is characteristic of the MCP and the fiber-optic taper and is independent of the MCP position. The calibration curve and the adjusted values of β_0 were then used to establish the wavelength scale for each MCP position. The accuracy of this wavelength scale is estimated to be 0.01 Å.

Since the MCP is flat and does not conform to the Rowland circle, the angular position β of the pixels is a nonlinear function of position on the MCP. The angular coverage of each pixel also varies across the MCP, and this means that the spectral resolution in the data recorded at the two ends of the MCP is different. This is a consideration when overlapping spectra recorded at adjacent MCP positions are pieced together to form a composite spectrum that covers a wide wavelength range. In order to correct for this effect, the pixel-bin positions were numerically transformed to be linear in β, and the angular width $\delta\beta$ of each bin was set equal to the original width of the tangential pixel. The counts were distributed into the new pixel bins based on the original angular widths of the pixels. As a result, the spectrum on one side of the tangential pixel was slightly stretched, and the spectrum on the other side was slightly compressed. The overlapping spectra from adjacent MCP positions can be aligned to an accuracy of 0.01 Å.

RESULTS

The spectra are shown in Figs. 3–11. The first-order spectrum is indicated by the solid line, and the first-order spectrum shifted to second- and third-order wavelengths is indicated by the dotted and the dashed lines, respectively. The strong spectral lines appear in multiple orders, and these lines provided a good independent check on the absolute wavelength scale.

Listed in Table 1 are the measured wavelengths and the classifications of the transitions. The overall accuracy of the measured wavelengths is estimated to be 0.02 Å. Also

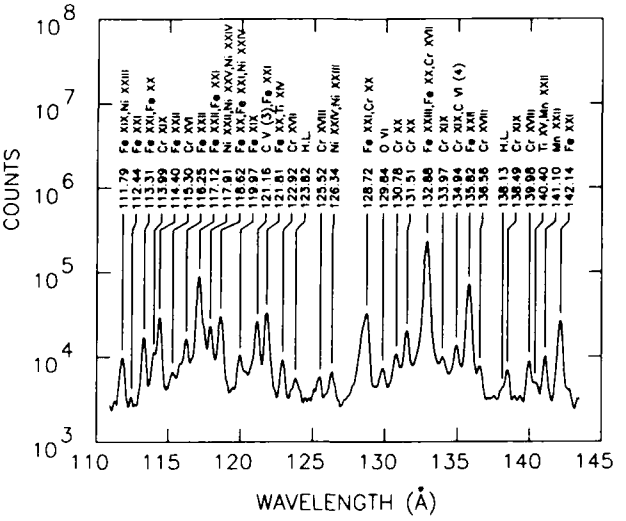

Fig. 4. The PLT spectrum for 110–145 Å.

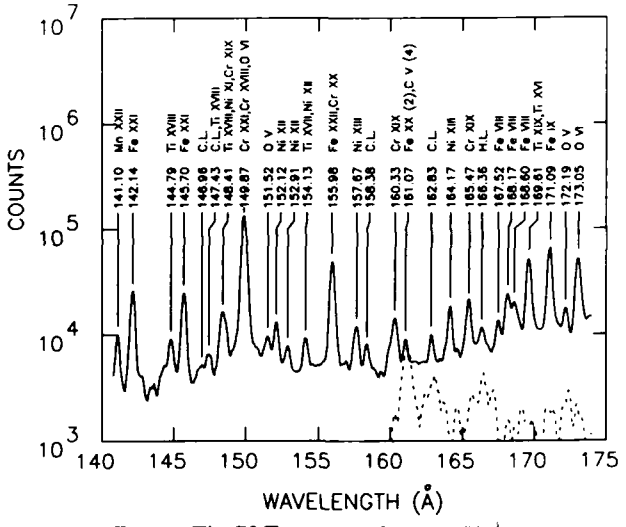

Fig. 5. The PLT spectrum for 140–175 Å.

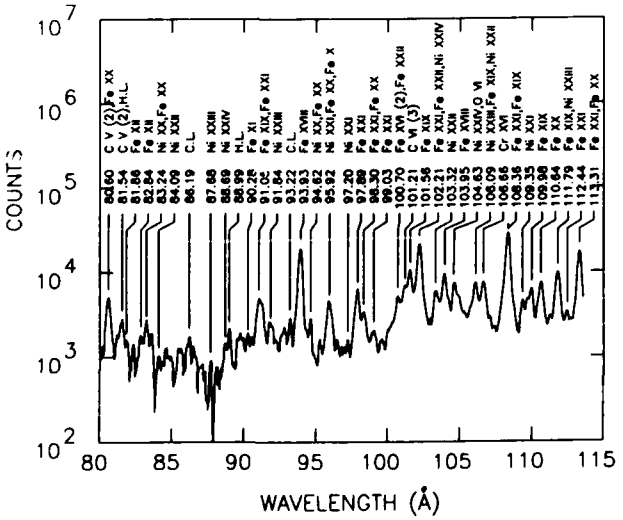

Fig. 3. The PLT spectrum for 80–115 Å.

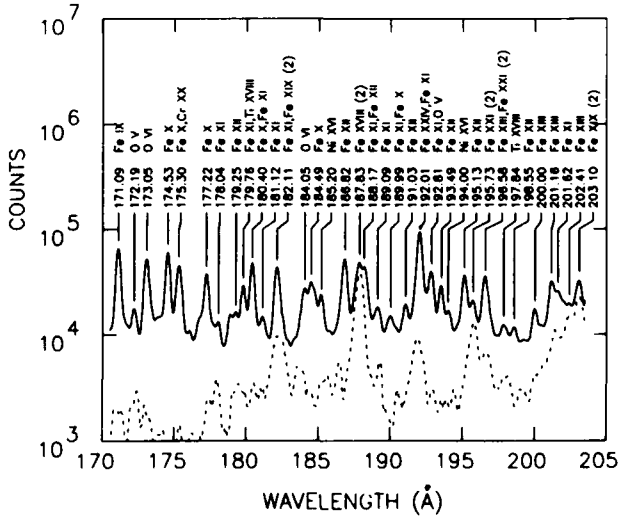

Fig. 6. The PLT spectrum for 170–205 Å.

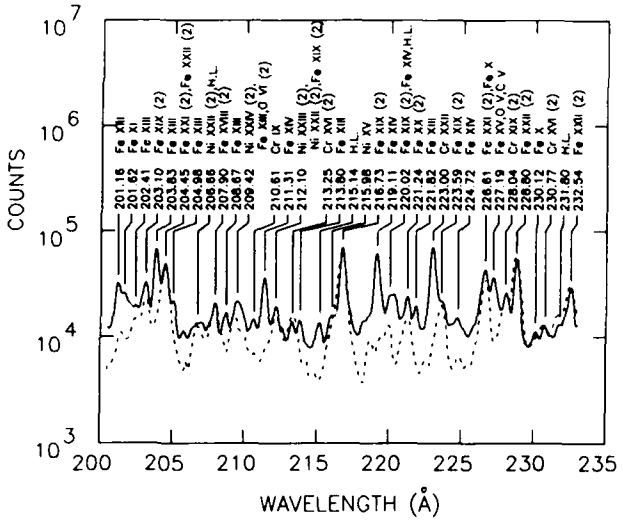

Fig. 7. The PLT spectrum for 200–235 Å.

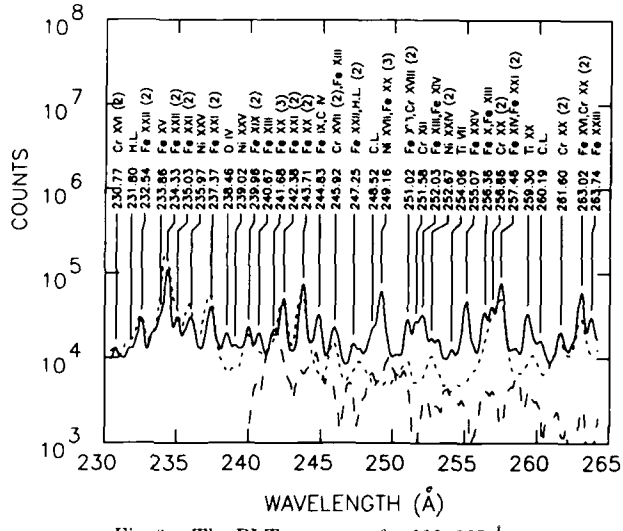

Fig. 8. The PLT spectrum for 230–265 Å.

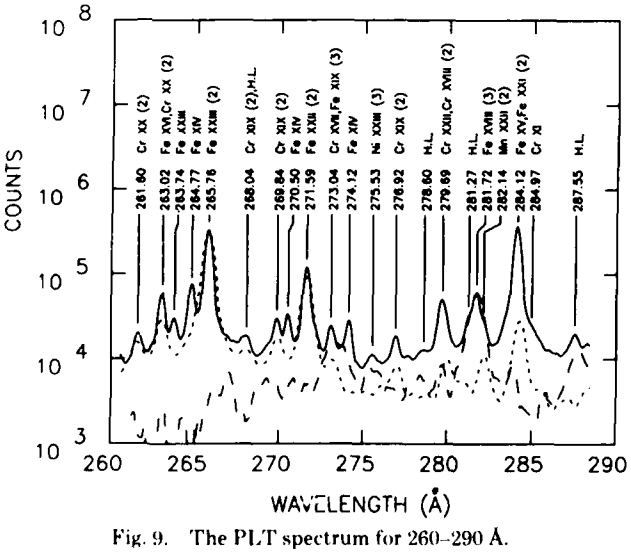

Fig. 9. The PLT spectrum for 260–290 Å.

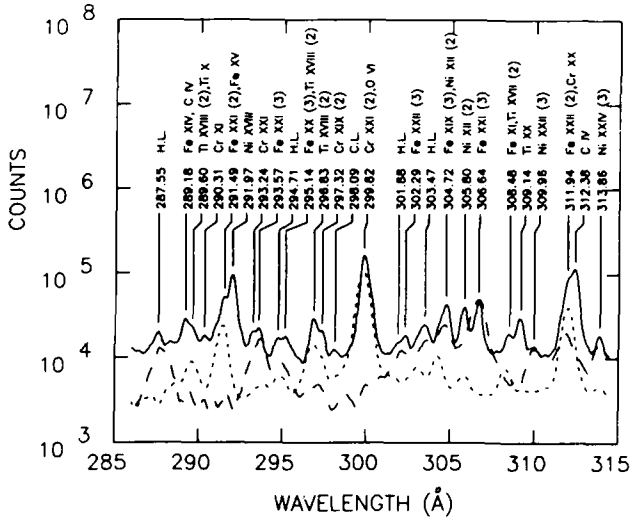

Fig. 10. The PLT spectrum for 285–315 Å.

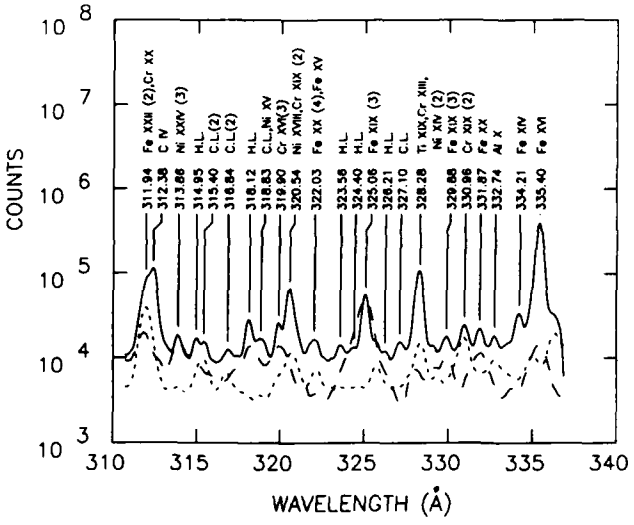

Fig. 11. The PLT spectrum for 310–340 Å.

Table 1. Wavelengths and Transitions 80–340 Å

Wavelength (Å)			
Present	Previous[a]	Ion[b]	Transition
80.17	80.23	Fe XII	$3p^3\ ^2D_{3/2}$–$3p^2(^1D)4s\ ^2D_{5/2}$
80.60	40.27(2)	C V	$1s^2\ ^1S_0$–$1s2p\ ^1P_1$
	80.49	Fe XX	$2s^22p^3\ ^4S_{3/2}$–$2s2p^4\ ^2P_{3/2}$
81.18		H.L.	
81.47	40.73(2)	C V	$1s^2\ ^1S_0$–$1s2p\ ^3P_1$
81.54		H.L.	
81.86bl	81.65	Fe XII	$3p^3\ ^2D_{3/2}$–$3p^2(^3P)4s\ ^2P_{3/2}$
	81.94	Fe XII	$3p^3\ ^2D_{5/2}$–$3p^2(^3P)4s\ ^2P_{3/2}$
82.32bl		C.L.	
82.84	82.84	Fe XII	$3p^3\ ^2P_{3/2}$–$3p^2(^1D)4s\ ^2D_{5/2}$
83.24	83.18	Ni XX	$2s^22p^5\ ^2P_{3/2}$–$2s2p^6\ ^2S_{1/2}$
	83.23	Fe XX	$2s^22p^3\ ^2D_{3/2}$–$2s2p^4\ ^2P_{1/2}$
83.58		H.L.	
84.09bl	84.07	Ni XXII	$2s^22p^3\ ^2D_{5/2}$–$2s2p^4\ ^2P_{3/2}$
84.57bl		H.L.	
85.59bl		H.L.	

Table 1. Continued

Wavelength (Å) Present	Previous[a]	Ion[b]	Transition
86.19		C.L.	
86.47		C.L.	
87.68	87.67	Ni XXIII	$2s^22p^2\,^3P_1$–$2s2p^3\,^3S_1$
88.11	88.11	Ni XXIII	$2s^22p^2\,^1D_2$–$2s2p^3\,^1P_1$
88.69bl	88.61	Ni XXIV	$2s^22p\,^2P_{1/2}$–$2s2p^2\,^2P_{3/2}$
88.99		H.L.	
89.73		H.L.	
90.28bl	90.21	Fe XI	$3p^4\,^3P_1$–$3p^3(^4S)4s\,^3S_1$
90.59bl	90.61	Fe XX	$2s^22p^3\,^2D_{3/2}$–$2s2p^4\,^2P_{3/2}$
91.05	91.02	Fe XIX	$2s^22p^4\,^1D_2$–$2s2p^5\,^1P_1$
91.27bl	91.27	Fe XXI	$2s^22p^2\,^3P_0$–$2s2p^3\,^3S_1$
91.84bl	91.87	Ni XXIII	$2s^22p^2\,^3P_2$–$2s2p^3\,^3S_1$
92.79		H.L.	
93.22		C.L.	
93.93	93.93	Fe XVIII	$2s^22p^5\,^2P_{3/2}$ – $2s2p^6\,^2S_{1/2}$
94.62	94.50	Ni XX	$2s^22p^5\,^2P_{1/2}$–$2s2p^6\,^2S_{1/2}$
	94.64	Fe XX	$2s^22p^3\,^2D_{3/2}$–$2s2p^4\,^2S_{1/2}$
95.25		H.L.	
95.92	95.86	Ni XXI	$2s^22p^4\,^3P_2$–$2s2p^5\,^3P_2$
	95.92	Fe XX	$2s^22p^3\,^4S_{3/2}$–$2s2p^4\,^2D_{3/2}$
96.12bl	96.12	Fe X	$3p^5\,^2P_{3/2}$–$3p^4(^3P)4s\,^2P_{3/2}$
96.45		H.L.	
96.77	96.80	Ni XXI	$2s^22p^4\,^3P_0$–$2s2p^5\,^3P_1$
97.20	97.15	Ni XXI	$2s^22p^4\,^1S_0$–$2s2p^5\,^1P_1$
97.89bl	97.86	Fe XXI	$2s^22p^2\,^3P_1$–$2s2p^3\,^3S_1$
98.30	98.36	Fe XXI	$2s^22p^2\,^1D_2$–$2s2p^3\,^1P_1$
	98.35	Fe XX	$2s^22p^3\,^2P_{3/2}$–$2s2p^4\,^2P_{1/2}$
99.03	99.02	Fe XXI	$2s^22p^2\,^3P_2$–$2s2p^3\,^1D_2$
100.25bl	100.24	Ni XXI	$2s^22p^4\,^3P_1$–$2s2p^5\,^3P_1$
100.70bl	50.35(2)	Fe XVI	$2p^63s\,^2S_{1/2}$–$2p^64p\,^2P_{3/2}$
	100.77	Fe XXII	$2s^22p\,^2P_{1/2}$–$2s2p^2\,^2P_{3/2}$
101.21	33.73(3)	C VI	$1s\,^2S_{1/2}$–$2p\,^2P_{1/2}$
	33.74(3)	C VI	$1s\,^2S_{1/2}$–$2p\,^2P_{3/2}$
101.56	101.56	Fe XIX	$2s^22p^4\,^3P_2$–$2s2p^5\,^3P_1$
102.21	102.21	Fe XXI	$2s^22p^2\,^3P_2$–$2s2p^3\,^3S_1$
	102.22	Fe XXII	$2s^22p\,^2P_{1/2}$–$2s2p^2\,^2P_{1/2}$
	102.10	Ni XXIV	$2s^22p\,^2P_{3/2}$–$2s2p^2\,^4P_{3/2}$
103.32	103.31	Ni XXII	$2s^22p^3\,^4S_{1/2}$–$2s2p^4\,^4P_{1/2}$
103.95	103.94	Fe XVIII	$2s^22p^5\,^2P_{1/2}$–$2s2p^6\,^2S_{1/2}$
104.63	104.63	Ni XXIV	$2s^22p\,^2P_{1/2}$–$2s2p^2\,^2S_{1/2}$
104.81bl	104.81	O VI	$2s\,^2S_{1/2}$–$5p\,^2P_{3/2}$
106.09	106.05	Ni XXIII	$2s^22p^2\,^3P_2$–$2s2p^3\,^3P_2$
	106.05	Ni XXII	$2s^22p^3\,^4S_{3/2}$–$2s2p^4\,^4P_{3/2}$
	106.11	Fe XIX	$2s^22p^4\,^1S_0$–$2s2p^5\,^1P_1$
106.32bl	106.32	Fe XIX	$2s^22p^4\,^3P_1$–$2s2p^5\,^3P_0$
106.66	106.63	Cr XVI	$2s^22p^5\,^2P_{3/2}$–$2s2p^6\,^2S_{1/2}$
108.11bl	108.11	Fe XXI	$2s^22p^2\,^3P_0$–$2s2p^3\,^3P_1$
108.36	108.36	Fe XIX	$2s^22p^4\,^3P_2$–$2s2p^5\,^3P_2$
109.35	109.31	Ni XXI	$2s^22p^4\,^3P_1$–$2s^22p^5\,^3P_2$
109.73		H.L.	
109.98	109.95	Fe XIX	$2s^22p^4\,^3P_0$–$2s2p^5\,^3P_1$
110.64	110.63	Fe XX	$2s^22p^3\,^2D_{3/2}$–$2s2p^4\,^2D_{3/2}$
111.79	111.70	Fe XIX	$2s^22p^4\,^3P_1$–$2s2p^5\,^3P_1$
	111.83	Ni XXIII	$2s^22p^2\,^3P_0$–$2s2p^3\,^3D_1$
112.44	112.45	Fe XXI	$2s^22p^2\,^1S_0$–$2s2p^3\,^1P_1$
113.31	113.29	Fe XXI	$2s^22p^2\,^1D_2$–$2s2p^3\,^1D_2$
	113.35	Fe XX	$2s^22p^3\,^2D_{5/2}$–$2s2p^4\,^2D_{5/2}$
113.99b	114.01	Cr XIX	$2s^22p^2\,^3P_2$–$2s2p^3\,^3S_1$
114.40	114.41	Fe XXII	$2s^22p\,^2P_{3/2}$–$2s2p^2\,^2P_{3/2}$
115.30	115.36	Cr XVI	$2s^22p^5\,^2P_{1/2}$–$2s2p^6\,^2S_{1/2}$
115.82	115.82	O VI	$2s\,^2S_{1/2}$–$4p\,^2P_{3/2}$
	115.83	O VI	$2s\,^2S_{1/2}$–$4p\,^2P_{1/2}$
116.25	116.27	Fe XXII	$2s^22p\,^2P_{3/2}$–$2s2p^2\,^2P_{1/2}$
117.12	117.18	Fe XXII	$2s^22p\,^2P_{1/2}$–$2s2p^2\,^2S_{1/2}$
117.49bl	117.49	Fe XXI	$2s^22p^2\,^3P_1$–$2s2p^3\,^3P_1$
117.91	117.92	Ni XXII	$2s^22p^3\,^4S_{3/2}$–$2s2p^4\,^4P_{5/2}$
	117.94[c]	Ni XXV	$2s^2\,^1S_0$–$2s2p\,^1P_1$
118.62	118.47	Ni XXIV	$2s^22p\,^2P_{1/2}$–$2s2p^2\,^2D_{3/2}$
	118.68	Fe XX	$2s^22p^3\,^4S_{3/2}$–$2s2p^4\,^4P_{1/2}$
	118.69	Fe XXI	$2s^22p^2\,^3P_1$–$2s2p^3\,^3P_0$
119.97	119.99	Fe XIX	$2s^22p^4\,^3P_1$–$2s2p^5\,^3P_2$
120.35	120.35	Ni XXI	$2s^22p^4\,^1D_2$–$2s2p^5\,^3P_2$
120.81bl	40.27(3)	C V	
121.16	121.19	Fe XXI	$2s^22p^2\,^3P_2$–$2s2p^3\,^3P_2$
121.81	121.85	Fe XX	$2s^22p^3\,^4S_{3/2}$–$2s2p^4\,^4P_{3/2}$
	121.99	Ti XIV	$2s^22p^5\,^2P_{3/2}$–$2s2p^6\,^2S_{1/2}$
122.92	122.97	Cr XVII	$2s^22p^4\,^3P_2$–$2s2p^5\,^3P_2$
123.82		H.L.	
125.52	125.52	Cr XVIII	$2s^22p^3\,^2D_{3/2}$–$2s2p^4\,^2D_{3/2}$
126.34	126.30	Ni XXIV	$2s^22p\,^2P_{3/2}$–$2s2p^2\,^2S_{1/2}$
126.59bl	126.59	Ni XXIII	$2s^22p^2\,^3P_1$–$2s2p^3\,^3D_2$
128.44bl	128.44	Cr XX	$2s^22p\,^2P_{3/2}$–$2s2p^2\,^2P_{3/2}$
128.72	128.73	Fe XXI	$2s^22p^2\,^3P_0$–$2s2p^3\,^3D_1$
129.84	129.79	O VI	$2p\,^2P_{1/2}$–$4d\,^2D_{3/2}$
	129.87	O VI	$2p\,^2P_{3/2}$–$4d\,^2D_{5/2}$
130.78	130.75	Cr XX	$2s^22p\,^2P_{3/2}$–$2s2p^2\,^2P_{1/2}$
131.51	131.57	Cr XX	$2s^22p\,^2P_{1/2}$–$2s2p^2\,^2S_{1/2}$
132.88[d]	132.88	Fe XXIII	$2s^2\,^1S_0$–$2s2p\,^1P_1$
	132.84	Fe XX	$2s^22p^3\,^4S_{3/2}$–$2s2p^4\,^4P_{5/2}$
	132.83	Cr XVII	$2s^22p^4\,^3P_1$–$2s2p^5\,^3P_2$
133.97bl	134.05	Cr XIX	$2s^22p^2\,^3P_1$–$2s2p^3\,^3P_1$
134.94	134.94	Cr XIX	$2s^22p^2\,^3P_1$–$2s2p^3\,^3P_0$
	33.74(4)	C VI	$1s\,^2S_{1/2}$–$2p\,^2P_{1/2,3/2}$
135.82	135.76	Fe XXII	$2s^22p\,^2P_{1/2}$–$2s2p^2\,^2D_{3/2}$
136.56	136.59	Cr XVIII	$2s^22p^4\,^4S_{3/2}$–$2s2p^4\,^4P_{1/2}$
138.13bl		H.L.	
138.49	138.52	Cr XIX	$2s^22p^4\,^3P_2$–$2s2p^3\,^3P_2$
139.98	139.97	Cr XVIII	$2s^22p^3\,^4S_{3/2}$–$2s2p^4\,^4P_{3/2}$
140.40	140.40	Ti XV	$2s^22p^4\,^3P_2$–$2s2p^5\,^3P_2$
141.10	141.09	Mn XXII	$2s^2\,^1S_0$–$2s2p\,^1P_1$
142.14	142.14	Fe XXI	$2s^22p^2\,^3P_1$–$2s2p^3\,^3D_2$
144.37bl		C.L.	
144.79	144.76	Ti XVIII	$2s^22p\,^2P_{3/2}$–$2s2p^2\,^2P_{3/2}$
145.70	145.70	Fe XXI	$2s^22p^2\,^3P_2$–$2s2p^3\,^3D_3$
146.96bl		C.L.	
147.43bl		C.L.	
147.60bl	147.60	Ti XVIII	$2s^22p\,^2P_{3/2}$–$2s2p^2\,^2P_{1/2}$
148.41	148.46	Ti XVIII	$2s^22p\,^2P_{1/2}$–$2s2p^2\,^2S_{1/2}$
	148.40	Ni XI	$3p^6\,^1S_0$–$3p^53d\,^1P_1$
148.66bl	148.66	Cr XIX	$2s^22p^2\,^3P_0$–$2s2p^3\,^3D_1$
149.87	149.89	Cr XXI	$2s^2\,^1S_0$–$2s2p\,^1P_1$
	149.82	Cr XVIII	$2s^22p^3\,^4S_{3/2}$–$2s2p^4\,^4P_{5/2}$
150.07bl	150.09	O VI	$2s\,^2S_{1/2}$–$3p\,^2P_{3/2}$
	150.12	O VI	$2s\,^2S_{1/2}$–$3p\,^2P_{1/2}$
151.52	151.5	O V	$2s2p\,^3P$–$2s4d\,^3D$
152.12	152.15	Ni XII	$3p^5\,^2P_{3/2}$–$3p^4(^3P)3d\,^2D_{5/2}$
152.91	152.94	Ni XII	$3p^5\,^2P_{1/2}$–$3p^4(^3P)3d\,^2P_{3/2}$
154.13	154.13	Ti XVII	$2s^22p^2\,^3P_1$–$2s2p^3\,^3P_0$
	154.17	Ni XII	$3p^5\,^2P_{3/2}$–$3p^4(^3P)3d\,^2P_{3/2}$
155.98	155.94	Fe XXII	$2s^22p\,^2P_{3/2}$–$2s2p^2\,^2D_{5/2}$
	155.98	Cr XX	$2s^22p\,^2P_{1/2}$–$2s2p^2\,^2D_{3/2}$
157.67	157.73	Ni XIII	$3s^23p^4\,^3P_2$–$3s^23p^33d\,^3D_3$
158.38		C.L.	
159.97bl	159.97	Ni XII	$3p^5\,^2P_{1/2}$–$3p^4(^3P)^2P_{3/2}$

(*continued overleaf*)

Table 1. Continued

Wavelength (Å)				Wavelength (Å)			
Present	Previous[a]	Ion[b]	Transition	Present	Previous[a]	Ion[b]	Transition
160.33	160.32	Cr XIX	$2s^22p^2\,^3P_1$–$2s2p^3\,^3D_2$	204.45	102.21(2)	Fe XXI	
161.07	80.49(2)	Fe XX			102.22(2)	Fe XXII	
	40.27(4)	C V		204.98	204.94	Fe XIII	$3p^3\,^3P_2$–$3p3d\,^3D_1$
162.83		C.L.		205.70		C.L.	
164.17	164.15	Ni XIII	$3s^23p^4\,^3P_2$–$3s^23p^33d\,^3P_2$	206.39bl		H.L.	
165.47	165.46	Cr XIX	$2s^22p^2\,^3P_2$–$2s2p^3\,^3D_3$	206.66bl	103.31(2)	Ni XXII	
166.36		H.L.		206.98bl		H.L.	
167.52	167.49	Fe VIII	$3p^63d\,^2D_{3/2}$–$3p^5[3d^2(^3F)]\,^2D_{3/2}$	207.90	103.94(2)	Fe XVIII	
168.17	168.17	Fe VIII	$3p^63d\,^2D_{5/2}$–$3p^5[3d^2(^3F)]\,^2D_{5/2}$	208.67	208.68	Fe XIII	$3p^2\,^1S_0$–$3p3d\,^1P_1$
168.60	168.55	Fe VIII	$3p^63d\,^2D_{5/2}$–$3p^5[3d^2(^3P)]\,^2P_{3/2}$	209.42bl	104.63(2)	Ni XXIV	
169.61	169.58	Ti XIX	$2s^2\,^1S_0$–$2s2p\,^1P_1$		209.62	Fe XIII	$3p^2\,^3P_1$–$3p3d\,^3P_2$
169.74bl	169.74	Ti XVI	$2s^22p^3\,^4S_{3/2}$–$2s2p^4\,^4P_{5/2}$		104.81(2)	O VI	
171.09	171.07	Fe IX	$3p^6\,^1S_0$–$3p^53d\,^1P_1$	209.92bl	209.92	Fe XIII	$3p^2\,^3P_2$–$3p3d\,^3P_1$
172.19	172.17	O V	$2s^2\,^1S_0$–$2s3p\,^1P_1$	210.61	210.62	Cr IX	$3p^4\,^3P_2$–$3p^3(^4S)3d\,^3D_3$
173.05	172.94	O VI	$2p\,^2P_{1/2}$–$3d\,^2D_{3/2}$	211.31	211.32	Fe XIV	$3p\,^2P_{1/2}$–$3d\,^2D_{3/2}$
	173.08	O VI	$2p\,^2P_{3/2}$–$3d\,^2D_{3/2}$	212.10	106.05(2)	Ni XXIII	
174.53	174.53	Fe X	$3p^5\,^2P_{3/2}$–$3p^4(^3P)3d\,^3D_{5/2}$		106.05(2)	Ni XXII	
175.30	175.26	Fe X	$3p^5\,^2P_{1/2}$–$3p^4(^3P)3d\,^2D_{3/2}$		106.11(2)	Fe XIX	
	175.36	Cr XX	$2s^22p\,^2P_{3/2}$–$2s2p^2\,^2D_{5/2}$	212.50bl		H.L.	
176.72bl		H.L.		213.25	106.63(2)	Cr XVI	
177.22	177.24	Fe X	$3p^5\,^2P_{3/2}$–$2p^4(^3P)3d\,^2P_{3/2}$	213.80	213.77	Fe XIII	$3p^2\,^3P_2$–$3p3d\,^3P_2$
178.04	178.06	Fe XI	$3p^4\,^3P_2$–$3p^3(^4S)3d\,^3D_2$	215.14		H.L.	
178.85		C.L.		215.98	215.94	Ni XV	$3s^23p^2\,^3P_1$–$3s3p^3\,^3S_1$
179.25	179.27	Fe XII	$3p^3\,^2D_{5/2}$–$3p^2(^3P)3d\,^2D_{5/2}$	216.73	108.36(2)	Fe XIX	
179.76	179.76	Fe XI	$3p^4\,^1D_2$–$3p^3(^2D)3d\,^1F_3$	218.26		C.L.	
	179.90	Ti XVIII	$2s^22p\,^2P_{1/2}$–$2s2p^2\,^2D_{3/2}$	219.11	219.12	Fe XIV	$3p\,^2P_{3/2}$–$3d\,^2D_{5/2}$
180.40	180.45	Fe X	$3p^5\,^2P_{1/2}$–$3p^43d(^3P)^2P_{1/2}$	220.02bl	109.95(2)	Fe XIX	
	180.40	Fe XI	$3p^4\,^3P_2$–$3p^3(^4S)3d\,^3D_3$		220.08	Fe XIV	$3p\,^2P_{3/2}$–$3d\,^2D_{3/2}$
181.12	181.14	Fe XI	$3p^4\,^3P_0$–$3p^3(^4S)3d\,^3D_1$	220.29bl		H.L.	
182.11	91.02(2)	Fe XIX		221.24	110.63(2)	Fe XX	
	182.17	Fe XI	$3p^4\,^3P_1$–$3p^3(^4S)3d\,^3D_2$	221.82	221.82	Fe XIII	$3p^2\,^1D_2$–$3p3d\,^1D_2$
182.52bl	91.27(2)	Fe XXI(2)		223.00	223.01	Cr XXII	$2s\,^2S_{1/2}$–$2p\,^2P_{3/2}$
184.05	183.94	O VI	$2p\,^2P_{1/2}$–$3s\,^2S_{1/2}$	223.59	111.70(2)	Fe XIX	
	184.12	O VI	$2p\,^2P_{3/2}$–$3s\,^2S_{1/2}$	224.72	224.75	Fe XV	$3p3d\,^3P_0$–$3s3d\,^3D_1$
184.49	184.54	Fe X	$3p^5\,^2P_{3/2}$–$3p^4(^1D)3d\,^2S_{1/2}$	226.30bl	226.30	Fe X	$3p^5\,^2P_{3/2}$–$3p^4(^1D)3d\,^2D_{5/2}$
185.20	185.23	Ni XVI	$3p\,^2P_{1/2}$–$3d\,^2D_{3/2}$	226.61	113.29(2)	Fe XXI	
186.82bl	186.86	Fe XII	$3p^3\,^2D_{3/2}$–$3p^2(^3P)3d\,^2F_{5/2}$	227.19	227.21	Fe XV	$3s3p\,^3P_1$–$3s3d\,^3D_2$
	186.88	Fe XII	$3p^3\,^2D_{5/2}$–$3p^2(^3P)3d\,^2F_{7/2}$		227.2	O V, C V	
187.83bl	93.93(2)	Fe XVIII		228.04	114.01(2)	Cr XIX	
188.17bl	188.17	Fe XII	$3p^3\,^2P_{1/2}$–$3p^2(^3P)3d\,^2D_{3/2}$	228.80	114.41(2)	Fe XXII	
	188.22	Fe XI	$3p^4\,^3P_2$–$3p^3(^2D)3d\,^3P_2$	230.12	230.09	Fe X	$3p^5\,^2P_{3/2}$–$3p^4(^1D)3d\,^2D_{3/2}$
189.09	189.13	Fe XI	$3p^4\,^3P_1$–$3p^3(^2D)3d\,^3P_1$	230.77	115.36(2)	Cr XVI	
189.99	189.94	Fe XI	$3p^4\,^3P_2$–$3p^3(2D)3d\,^1P_1$	231.80bl		H.L.	
	190.04	Fe X	$3p^5\,^2P_{1/2}$–$3p^4(^1D)3d\,^2S_{1/2}$	232.54	116.27(2)	Fe XXII	
191.03	191.04	Fe XII	$3p^3\,^2P_{3/2}$–$3p^2(^3P)3d\,^2D_{5/2}$	233.32bl		H.L.	
192.01	192.01	Fe XXIV	$2s\,^2S_{1/2}$–$2p\,^2P_{3/2}$	233.86bl	233.86	Fe XV	$3s3p\,^3P_2$–$3s3d\,^3D_3$
	192.02	Fe XI	$3p^4\,^3P_1$–$3p^3(^2D)3d\,^3S_1$	234.33	117.18(2)	Fe XXII	
192.81	192.82	Fe XI	$3p^4\,^3P_1$–$3p^3(^2D)3d\,^3P_2$	235.03	117.49(2)	Fe XXI	
	192.8	O V	$2s2p\,^3P$–$2s3d\,^3D$	235.97bl	117.94(2)[c]	Ni XXV	
193.49	193.51	Fe XII	$3p^3\,^4S_{3/2}$–$3p^2(^3P)3d\,^4P_{3/2}$	237.37	118.69(2)	Fe XXI	
194.00	194.04	Ni XVI	$3p\,^2P_{3/2}$–$3d\,^2D_{5/2}$	238.46	238.36	O IV	$2p\,^2P_{1/2}$–$3d\,^2D_{3/2}$
195.13	195.12	Fe XII	$3p^3\,^4S_{3/2}$–$3p^2(^3P)3d\,^4P_{5/2}$		238.57	O IV	$2p\,^2P_{3/2}$–$3d\,^2D_{5/2}$
195.73	97.86(2)	Fe XXI		239.02	238.86	Ni XXV	$2s^2\,^1S_0$–$2s2p\,^3P_1$
196.58	196.53	Fe XIII	$3p^2\,^1D_2$–$3p3d\,^1F_3$	239.96	119.99(2)	Fe XIX	
	98.36(2)	Fe XXI		240.67	240.71	Fe XIII	$3s^23p^2\,^3P_0$–$3s3p^3\,^3S_1$
197.84	197.82	Ti XVIII	$2s^22p\,^2P_{3/2}$–$2s2p^2\,^2D_{5/2}$	241.68	80.49(3)	Fe XX	
198.55	198.58	Fe XII	$3p^3\,^2P_{1/2}$–$3p^2(1D)3d\,^2P_{3/2}$	242.38	121.19(2)	Fe XXI	
200.00	200.02	Fe XIII	$3p^2\,^3P_1$–$3p3d\,^3D_2$	243.71	121.85(2)	Fe XX	
201.16bl	201.12	Fe XIII	$3p^2\,^3P_1$–$3p3d\,^3D_1$	244.83	244.91	Fe IX	$3p^6\,^1S_0$–$3p^53d\,^3P_1$
201.62bl	201.58	Fe XI	$3p^4\,^3P_2$–$3p^3(^2P)\,^3P_2$		244.91	C IV	$2s\,^2S_{1/2}$–$4p\,^2P_{3/2}$
202.02bl	202.04	Fe XIII	$3p^4\,^3P_0$–$3p3d\,^3P_1$	245.92	122.97(2)	Cr XVII	
202.41bl	202.42	Fe XIII	$3p^4\,^3P_1$–$3p3d\,^3P_0$	246.21bl	246.21	Fe XIII	$3s^23p^2\,^3P_1$–$3p^33d\,^3S_1$
203.10bl	101.56(2)	Fe XIX		247.25	247.20	Fe XXII	$2s^22p\,^2P_{1/2}$–$2s2p^2\,^4P_{1/2}$
203.83	203.83	Fe XIII	$3p^4\,^3P_2$–$3p3d\,^3D_3$	247.65	123.82(2)	H.L.	

Table 1. Continued

Wavelength (Å)		Ion[b]	Transition
Present	Previous[a]		
248.52		C.L.	
249.16	249.18	Ni XVII	$3s^2\,{}^1S_0$–$3s3p\,{}^1P_1$
249.54bl	83.18(3)	Fe XX	
251.02	125.52(2)	Cr XVIII	
	251.07	Fe XVI	$3p\,{}^2P_{1/2}$–$3d\,{}^2D_{3/2}$
251.58	251.52	Cr XII	$3p\,{}^2P_{3/2}$–$3d\,{}^2D_{5/2}$
252.03	251.95	Fe XIII	$3s^23p^2\,{}^3P_2$–$3s3p^3\,{}^3S_1$
	252.19	Fe XIV	$3s^23p\,{}^2P_{1/2}$–$3s3p^2\,{}^2P_{3/2}$
252.67	126.30(2)	Ni XXIV	
253.09		C.L.	
254.06bl	254.02	Ti VII	$3p^4\,{}^3P_2$–$3p^3(^4S)3d\,{}^3D_3$
255.07	255.08	Fe XXIV	$2s\,{}^2S_{1/2}$–$2p\,{}^2P_{1/2}$
256.36	256.38	Fe X	$3p^5\,{}^2P_{3/2}$–$3p^4(^3P)3d\,{}^4D_{3/2}$
	256.42	Fe XIII	$3s^23p^2\,{}^1D_2$–$3s3p^3\,{}^1P_1$
256.86	128.42(2)	Cr XX	
257.46	257.39	Fe XIV	$3s^23p\,{}^2P_{1/2}$–$3s3p^2\,{}^2P_{1/2}$
	128.73(2)	Fe XXI	
259.30	259.29	Ti XX	$2s\,{}^2S_{1/2}$–$2p\,{}^2P_{3/2}$
260.19		C.L.	
261.60	130.75(2)	Cr XX	
263.02	262.97	Fe XVI	$3p\,{}^2P_{3/2}$–$3d\,{}^2D_{5/2}$
	131.57(2)	Cr XX	
263.74	263.74	Fe XXIII	$2s^2\,{}^1S_0$–$2s2p\,{}^3P_1$
264.77	264.79	Fe XIV	$3s^23p\,{}^2P_{3/2}$–$3s3p^2\,{}^2P_{3/2}$
265.76	132.88(2)	Fe XXIII	
267.79bl		H.L.	
268.04bl	134.05(2)	Cr XIX	
269.84	134.94(2)	Cr XIX	
270.50	270.52	Fe XIV	$3s^22p\,{}^2P_{3/2}$–$3s3p^2\,{}^2P_{1/2}$
271.59	135.76(2)	Fe XXII	
273.04	136.59(2)	Cr XVII	
	91.02(3)	Fe XIX	
274.12	274.20	Fe XIV	$3s^23p\,{}^2P_{1/2}$–$3s3p^2\,{}^2S_{1/2}$
275.53bl	91.87(3)	Ni XXIII	
276.92	138.52(2)	Cr XIX	
278.60		H.L.	
279.69	279.72	Cr XXII	$2s\,{}^2S_{1/2}$–$2p\,{}^2P_{1/2}$
	139.87(2)	Cr XVIII	
281.27bl		H.L.	
281.72	93.93(3)	Fe XVIII	
282.14bl	141.09(2)	Mn XXII	
283.64bl	283.64	Fe XII	$3s^23p^3\,{}^2D_{3/2}$–$3s3p^4\,{}^2P_{1/2}$
284.12	284.15	Fe XV	$3s^2\,{}^1S_0$–$3s3p\,{}^1P_1$
284.28bl	142.14(2)	Fe XXI	
284.97bl	284.97	Cr XI	$3s^23p^2\,{}^3P_1$–$3s3p^3\,{}^3S_1$
287.55		H.L.	
289.18	289.16	Fe XIV	$3s^23p\,{}^2P_{3/2}$–$3s3p^2\,{}^2S_{1/2}$
	289.2	C IV	$2p\,{}^2P$–$4d\,{}^2D$
289.60bl	144.76(2)	Ti XVIII	
	289.58	Ti X	$3p\,{}^2P_{1/2}$–$3d\,{}^2D_{3/2}$
290.33	290.31	Cr XI	$3s^23p^2\,{}^3P_2$–$3s3p^3\,{}^3S_1$
291.01bl	291.01	Fe XII	$3s^23p^3\,{}^2D_{5/2}$–$3s3p^4\,{}^2P_{3/2}$
291.49	145.70(2)	Fe XXI	
291.97	292.00	Ni XVIII	$3s\,{}^2S_{1/2}$–$3p\,{}^2P_{3/2}$
293.24bl	293.16	Cr XXI	$2s^2\,{}^1S_0$–$2s2p\,{}^3P_1$
293.57	97.86(3)	Fe XXI	
294.71bl		H.L.	
295.14bl	98.35(3)	Fe XX	
	147.56(2)	Ti XVIII	
295.58bl	295.58	Ti X	$3p\,{}^2P_{3/2}$–$3d\,{}^2D_{5/2}$
296.83	148.46(2)	Ti XVIII	
297.32bl	148.66(2)	Cr XIX	
298.09		C.L.	
299.82	149.89(2)	Cr XXI	
300.27bl	150.12(2)	O VI	
301.88bl		H.L.	
302.29	100.77(3)	Fe XXII	
302.93bl	151.52(2)	O V	
303.47bl		H.L.	
304.32	152.15(2)	Ni XII	
304.72	101.56(3)	Fe XIX	
305.80	152.94(2)	Ni XII	
306.64	102.21(3)	Fe XXI	
308.48bl	154.13(2)	Ti XVII	
	308.54	Fe XI	$3s^23p^4\,{}^1D_2$–$3s3p^5\,{}^1P_1$
309.14	309.09	Ti XX	$2s\,{}^2S_{1/2}$–$2p\,{}^2P_{1/2}$
309.96	103.31(3)	Ni XXII	
311.94bl	155.94(2)	Fe XXII	
	155.98(2)	Cr XX	
312.38	312.42	C IV	$2s\,{}^2S_{3/2}$–$3p\,{}^2P_{3/2}$
	312.43	C IV	$2s\,{}^2S_{1/2}$–$3p\,{}^2P_{1/2}$
313.86	104.63(3)	Ni XXIV	
314.95		H.L.	
315.40	157.67(2)	C.L.	
316.84	158.38(2)	C.L.	
318.12bl		H.L.	
318.83bl	318.67	C.L.	
	319.01	Ni XV	$3s^23p^2\,{}^3P_2$–$3s3p^3\,{}^3D_3$
319.90	106.63(3)	Cr XVI	
320.54bl	320.55	Ni XVIII	$3s\,{}^2S_{1/2}$–$3p\,{}^2P_{1/2}$
	160.32(2)	Cr XIX	
321.78bl	321.78	Fe XV	$3s3p\,{}^3P_2$–$3p^2\,{}^3P_1$
322.03bl	80.49(4)	Fe XX	
323.56		H.L.	
324.40		H.L.	
325.06	108.36(3)	Fe XIX	
325.68	162.83(2)	C.L.	
326.21		H.L.	
327.10bl		C.L.	
328.28	328.34	Ti XIX	$2s^2\,{}^1S_0$–$2s2p\,{}^3P_1$
	328.29	Cr XIII	$3s^2\,{}^1S_0$–$3s3p\,{}^1P_1$
	164.15(2)	Ni XIV	
329.88	109.95(3)	Fe XIX	
330.96	165.46(2)	Cr XIX	$2s^22p^2\,{}^3P_2$–$2s2p^3\,{}^3D_3$
331.87	110.63(3)	Fe XX	
332.74	332.77	Al X	$2s^2\,{}^1S_0$–$2s2p\,{}^1P_1$
334.21	334.17	Fe XIV	$3s^23p\,{}^2P_{1/2}$–$3s3p^2\,{}^2D_{3/2}$
335.40	335.40	Fe XVI	$3s\,{}^2S_{1/2}$–$3p\,{}^2P_{3/2}$

[a] The previously measured wavelengths are from Refs. 9–15.
[b] H.L., hot line; C.L., cold line.
[c] Independent measurement by E. Hinnov is 117.99 Å.
[d] Independent measurement by E. Hinnov is 132.913 Å.

listed in Table 1 are previously measured or calculated wavelengths from Refs. 9–16.

A number of lines are unidentified in Table 1. From the time dependence of the intensities of these lines, it could be determined that an unknown transition was from an ion that was abundant early in the discharge or during the plateau regime, and these lines are labeled cold line (C.L.) and hot line (H.L.), respectively.

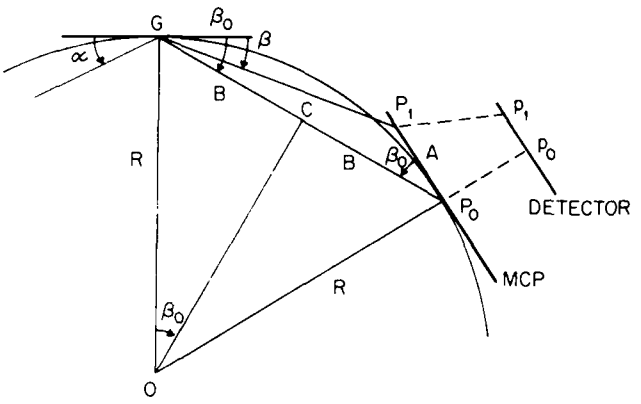

Fig. 12. The geometry of the spectrometer showing the grating G and the flat microchannel plate MCP. The angle of incidence is α. The angular position of the point on the MCP that is tangent to the Rowland circle is β_0, and p_0 is the pixel corresponding to the tangential point P_0. The distance to arbitrary point P_1 is A, and β is the angle of diffraction at this point.

CONCLUSIONS

Numerical techniques were developed to analyze the spectral data from the 2-m Schwob–Fraenkel spectrometer fitted with a flat MCP. By using reference spectral lines, the positions of the MCP were precisely determined, and corrections were made for the various nonlinearities in the recorded data. By using a pixel calibration curve, a wavelength scale was established with an accuracy of 0.01 Å, and the wavelengths of the spectral features were measured to an overall accuracy of 0.02 Å. A large number of ground-state transitions in Ti, Cr, Mn, Fe, and Ni were identified.

APPENDIX A

The geometry of the MCP, the fiber optic, and the detector is shown in Fig. 12. Point P_0 on the MCP is tangent to the Rowland circle, and this point corresponds to pixel number p_0 on the detector. The arbitrary point P_1 on the MCP corresponds to pixel number p_1. If M is the magnification of the fiber optic and N is the number of pixels per unit length on the detector, then the distance between points P_0 and P_1 on the MCP is

$$A = (p_1 - p_0)M/N. \tag{A1}$$

From the right triangle GOC,

$$B = R \sin \beta_0, \tag{A2}$$

where B is half of the distance from the center of the grating to the tangential point of the MCP, β_0 is the angular position of the tangential point, and R is the radius of the Rowland circle. Applying the law of sines to triangle GP_1P_0,

$$A/\sin(\delta\beta) = 2B/\sin(\pi - \beta_0 - \delta\beta), \tag{A3}$$

where $\delta\beta = \beta_0 - \beta$ is the angular position of point P_1 measured from the tangential point P_0. Solving Eq. (A3) for β and using Eqs. (A1) and (A2),

$$\beta = \beta_0 - \cot^{-1}[2RN/(p_0 - p_1)M - \cot \beta_0] \qquad \text{for } p_1 < p_0, \tag{A4}$$

$$\beta = \beta_0 + \cot^{-1}[2RN/(p_1 - p_0)M + \cot \beta_0] \qquad \text{for } p_1 > p_0. \tag{A5}$$

For each MCP position, a calibration curve similar to Fig. 2 was generated. The expected pixel positions of the standard lines were calculated from Eqs. (A4) and (1) by using the experimental values of the angular positions β_0 of the MCP. Small adjustments to the β_0 values were made so that the data points from all the MCP positions fell on the same smooth curve. The adjustments to β_0 were within the experimental uncertainties in the measured positions of the MCP. A polynomial function was fitted to the data points, as shown in Fig. 2, and this calibration curve was used to measure the wavelengths of the unknown lines.

ACKNOWLEDGMENT

This research was supported by the U.S. Defense Nuclear Agency.

* Permanent address, Racah Institute, Hebrew University of Jerusalem, Jerusalem, Israel.

REFERENCES AND NOTES

1. S. Suckewer, "Spectroscopic diagnostics of tokamak plasmas," Phys. Scr. **23,** 72 (1981).
2. S. Suckewer and E. Hinnov, "Iron forbidden lines in tokamak discharges," Phys. Rev. A **20,** 578 (1979).
3. B. C. Stratton, H. W. Moss, S. Suckewer, U. Feldman, J. F. Seely, and A. K. Bhatia, "Relative intensities of $2s^22p^k$–$2s2p^{k+1}$ transitions in F I- to B I-like Ti, Cr, Fe, Ni, and Ge in a tokamak plasma: a comparison of experiment and theory," Phys. Rev. A **31,** 2534 (1985).
4. A. S. Filler, J. L. Schwob, and B. S. Fraenkal, in *Proceedings of the 5th International Conference on UV Radiation Physics, Castex*, M. Pouey and N. Pouey, eds. (Centre National de la Recherche Scientifique, Paris, 1977), Vol. 1, p. 86.
5. J. L. Schwob, A. Wouters, S. Suckewer, and M. Finkenthal, "Time-resolving multichannel soft x-ray spectrometer for tokamak plasma diagnostics," Bull. Am. Phys. Soc. **28,** 1252 (1983).
6. J. L. Schwob, A. Wouters, S. Suckewer, F. P. Boody, and M. Finkenthal, "Time-resolved spectra in the 5–300 Å region emitted from the PLT and TFTR tokamak plasmas," in *Proceedings of the 8th International Colloquium on EUV and X-Ray Spectroscopy of Astrophysical and Laboratory Plasmas*, IAU Coll. No. 86 (U.S. Naval Research Laboratory, Washington, D.C., 1984).
7. A. W. Wouters, J. L. Schwob, F. P. Boody, and S. Suckewer, "Impurity radiation in TFTR in the 5–300 Å spectral region using a high resolution multichannel spectrometer," Bull. Am. Phys. Soc. **29,** 1303 (1984).
8. J. H. Davé, U. Feldman, J. F. Seely, A. Wouters, E. Hinnov, and S. Suckewer, "Time-resolved spectra in the 80–330 Å wavelength region from PLT tokamak plasmas," Rev. Sci. Instrum. **57,** 2058 (1986).
9. B. Edlén, "Comparison of theoretical and experimental level values of the $n = 2$ complex in ions isoelectronic with Li, Be, O, and F," Phys. Scr. **28,** 51 (1983).
10. B. Edlén, "Comparison of theoretical and experimental level values of the $n = 2$ configuration in the boron I isoelectronic sequence," Phys. Scr. **28,** 483 (1983).
11. B. Edlén, "Comparison of theoretical and experimental level values of the $n = 2$ configuration in the carbon I isoelectronic sequence," Phys. Scr. **31,** 345 (1985).
12. B. Edlén, "Comparison of theoretical and experimental level values of the $n = 2$ configurations in the nitrogen I isoelectronic sequence," Phys. Scr. **30,** 135 (1984).

13. W. E. Behring, L. Cohen, U. Feldman, and G. A. Doschek, "The solar spectrum: wavelengths and identifications from 160 to 770 angstroms," Astrophys. J. **203,** 521 (1976).
14. W. L. Wiese, *Spectroscopic Data for Iron* (Controlled Fusion Data Center, Oak Ridge National Laboratory, Oak Ridge, Tenn., 1985).
15. R. L. Kelly and L. J. Palumbo, "Atomic and ionic emission lines below 2000 angstroms," Rep. 7599 (Naval Research Laboratory, Washington, D.C., 1973).
16. Independent measurements of wavelengths in Table 1 were made by E. Hinnov in 1986.